Frictional wave dissipation in macro-roughness environments: a comparison of bottom stress and bulk canopy drag models

Solène Dealbera, Damien Sous

Frictional wave dissipation in macro-roughness environments: a comparison of bottom stress and bulk canopy drag models

Solène Dealbera[a,b,*], Damien Sous[a]

[a] *Université de Pau et des Pays de l'Adour, E2S-UPPA, SIAME, Anglet, France*
[b] *IMT Atlantique, Lab-STICC, UMR CNRS 6285, Brest, France*

Abstract

Friction dissipation induced by the seabed is a key factor for wave attenuation in nearshore environments presenting large roughness structures, such as rocky or coral shores. Two seminal models are classically used to predict bottom friction dissipation: the bottom stress (BS) and bulk canopy drag (BCD) models. Aiming to compare the performances of both models in controlled laboratory conditions, the present paper reanalyses the wave dissipation data provided by Dealbera et al. (2024). An approach to calculate the frontal transverse area based on real terrain consideration is suggested. The hydraulic parameter and the drag coefficient are optimized from the experimental data using several approaches and model parameterizations. Performance estimators of each model parameterization are compared and reveal a more robust predictive performance of the BCD model. The BS model could be improved by changing the vertical reference of the estimated flow velocity.

Keywords: Waves, Macro-roughness, Friction, Canopy, Model

1. Introduction

Facing climate change and ever-increasing anthropization, nearshore areas are particularly vulnerable to extreme events that generate coastal floodings and intensified erosion (Vousdoukas et al., 2020; Kirezci et al., 2020). In order to correctly predict the wave-driven coastal hazards for coastal engineering and citizen safety needs, the development of accurate wave models has been a major focus of the last four decades. Modeling the wave propagation and transformation in nearshore areas requires representing a series of physical processes driven by the shallowing bathymetry, including shoaling, refraction, diffraction, reflection, non-linear energy transfers and wave dissipation by breaking or bottom friction (Svendsen, 2005; Sous et al., 2021).

*Corresponding author: solene.dealbera@univ-pau.fr

A growing research effort is engaged to better characterize and predict wave transformation over rough seabeds, including coral reefs (Lowe et al., 2005a, 2007; Quiroga and Cheung, 2013; Monismith et al., 2015; Van Dongeren et al., 2013; Rogers et al., 2016; Sous et al., 2023) or rocky beaches (Farrell et al., 2009; Ogawa et al., 2015; Poate et al., 2018; Gon et al., 2020; Lavaud et al., 2020; Marques et al., 2024b). The standard approach for bottom frictional dissipation in spectral wave models relies on the assumption that roughness elements remain small w.r.t the bottom boundary layer thickness (Madsen, 1995). Such bottom stress models, hereinafter referred to as BS models, are based on a wave friction factor f_w, which can be predicted from the ratio between the near-bed wave orbital amplitude and a length-scale characterizing the roughness field, namely the hydraulic roughness (Swart, 1974; Soulsby et al., 1993; Madsen, 1995; Sous et al., 2023; Dealbera et al., 2024). Using field- and laboratory-calibrated formulations for f_w, BS models have been shown to remain usable for highly rough terrain (Gon et al., 2020; Dealbera et al., 2024), where the initial theoretical framework is likely no more valid. The general question about the limits of validity of BS models for macro-roughness conditions, i.e. for which roughness elements widely protrude above the bottom boundary layer, or mega-roughness conditions, i.e. for which roughness elements emerge, remains asked.

An alternative approach to represent the dissipative effect of rigid obstacles in wave-driven flow is to consider the drag force applied on the fluid volume (Dalrymple et al., 1984; Kobayashi et al., 1993). This approach is hereinafter referred to as the bulk canopy drag (BCD) model. Widely used to represent wave transformation around submerged structures such as oil platforms or vegetated seabeds (Mendez and Losada, 2004), BCD models are based on the general assumption of a network of identical rigid structures, usually cylinders. BCD models are based on the general assumption of a network of identical rigid structures, usually cylinders. (Mendez and Losada, 2004) mentioned that their formula was applicable to flexible plants by changing the value of the bulk drag coefficient to cover the ignorance of the plant motion. Since then, many studies have been devoted to the characterization of bulk drag coefficient both for rigid and flexible obstacles, including the coefficient dependency on the obstacle features, such as the geometry, distribution, deformation, and on the local hydrodynamical regimes described by dimensionless numbers, being generally the Reynolds number (Re) or the Keulegan Carpenter (KC) (see e.g. Kobayashi et al. (1993); Mendez and Losada (2004); Koftis et al. (2013); Anderson and Smith (2014); Ozeren et al. (2014); Losada et al. (2016); Chastel et al. (2020); Yin et al. (2024)). Note that both BS and BCD models have been implemented into frequency-integrated, spectral and phase-resolved models.

The present paper aims to compare and discuss the ability of BS and BCD models to represent wave dissipation in macro- to mega-roughness conditions. Yet BS and BCD models are generally used by distinct communities, to represent wave dissipation over rocky/coral and vegetated seabeds, respectively. BS models are expected to show degraded performance

for growing roughness height Dealbera et al. (2024). By contrast, the BCD model should be conceptually more capable to account for the roughness effect over the whole water column. However, standard BCD models are strictly designed for the idealized configuration of cylinder arrays. While easily applicable to seagrass or mangrove fields where characteristic vegetation height, diameter and density can be directly identified, BCD models remain questionable for real rocky or coral reef terrains where the roughness structure presents a fractal dimension with no defined roughness structure spacing and arrangement (Duvall et al., 2019; Stewart et al., 2019; Sous et al., 2020, 2024). Therefore, neither filling the condition for small roughness features compared to the boundary layer thickness required for BS models nor showing the regular arrangement of elongated obstacles, realistic macro- and mega-rough terrains fall in an ambiguous and sparsely documented range of seabed topography in terms of wave dissipation (Monismith et al., 2015; Dodet et al., 2018; Marques et al., 2024b,a). While widely documented in their specific validity domain, the assessment of the respective performances of BS and BCD models remains a challenging issue in macro- and mega-roughness environments, such as the cyclopean blocks of the Banneg island or the Flysch rocky outcrops of the Socoa platform (Sous et al., 2024), due to the scarcity of field data on wave transformation.

The series of experiments presented in Dealbera et al. (2024) characterizes a substantial range of idealized rough seabeds, from small roughness to macro-roughness in a hydrodynamically controlled environment. In this study, we intend to reuse this data (i) to develop an approach for the BCD model applicable to real rocky or coral reef terrain based on usable bed metrics, (ii) to compare the performances of various parameterizations of each model and, (iii), to identify the validity limits of each model. The first section recalls the experimental setup, the data processing, the theoretical models of the roughness-induced dissipation and their parameterizations. The second section presents the results, including the comparison of the performances of both models, while the Discussion section summarizes the observations and their limitations and provides prospects for future research works.

2. Methods

2.1. Experiments

The free surface elevation data used here come from the series of experiments carried out in the CASH wave flume (SeaTech, University of Toulon) and described in details by Dealbera et al. (2024). The flume is made of glass, 6m long and 0.5m wide, and equipped with a linearly sloping bed of 1/20. A piston wave-maker, with an absorbing system at the back, was used to generate waves on the 1m-long horizontal bottom section before the sloping bed. Five irregular wave conditions were generated from a JONSWAP spectrum with significant offshore wave heights varying from 0.047 to 0.075 m and peak periods ranging from

1 to 1.2 s. Each wave condition was first run over a beach with a 1/20 slope recovered with stainless steel plates that mimicked a smooth seabed reference (RF case). Each wave run was then repeatedly run over 26 seabed layouts created using LEGO® blocks set up on the slope. Several patterns were selected to identify the effects of the geometric structure of the roughness by varying the block heights, lengths and streamwise dimensions, the spacing and shifts between block rows. Appendix A displays an illustrative series of layouts. Free surface elevations were recorded using a series of resistive gauges along the cross-shore axis as shown in Figure 1. A fast Fourier Transform was then performed to extract H_{rms} the spectral root mean square height of the incident short waves over the $\frac{f_p}{2} < f < 3f_p$ frequency band, where f_p is the frequency peak, using the following formula: $H_{rms} = \sqrt{8 \int E(f) df}$, with $E(f)$ the spectral energy density.

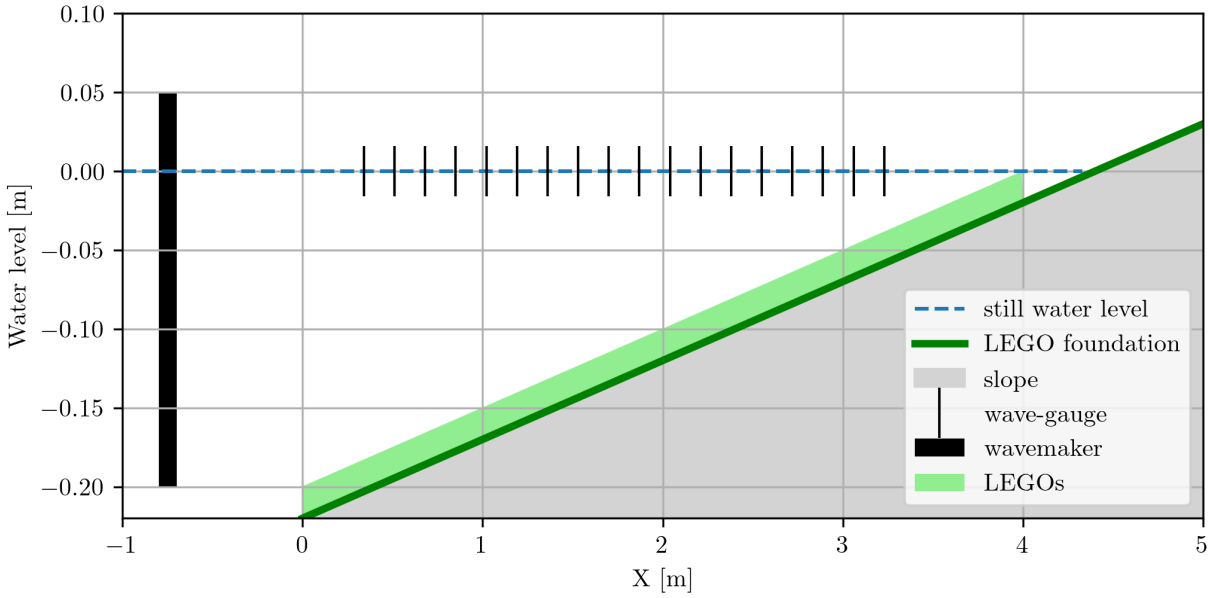

Figure 1: Diagram of the wave flume setup and instrumentation

The experimental scaling has been primarily designed to preserve relevant dimensionless numbers for wave propagation and breaking in nearshore area. The surf similarity parameter ranges from 0.12 to 0.6, while kh at the breaking point ranges from 0.4 to 0.65 (k and h between local wave number and depth). Due to the scale distortion between horizontal and vertical directions, the forced waves are necessarily non-linear, ka being of the order of 0.15 at the breaking point (a being the local wave amplitude), i.e. higher than values typically reached on gently sloping beaches. However, previous results on the same experimental

setup (Sous et al., 2021; Dealbera et al., 2024) and the present observations demonstrated that standard linear wave models remain relevant for the present range of wave case, i.e. the effect of the departure from linear wave assumption remains small compared to the monitored processes, and consistent with existing laboratory and field observations.

2.2. Performance estimators

Two classical estimators are used hereafter to quantify the accuracy of the agreement between observations and model predictions: the normalized root mean square error (NRMSE) based on the normalization of the root mean square error (RMSE) and the Willmott index (WI) which shows a standardized error measure between 0 and 1:

$$RMSE = \sqrt{\frac{1}{n}\sum_{i}^{n}\left(\hat{\Theta}_i - \Theta_i\right)^2} \tag{1}$$

$$NRMSE = \frac{RMSE}{\sigma\left(\Theta\right)} \tag{2}$$

$$WI = 1 - \frac{\sum_i^n \left(\hat{\Theta}_i - \Theta_i\right)^2}{\sum_i^n \left(\left|\hat{\Theta}_i - \overline{\Theta}\right| + \left|\Theta_i - \overline{\Theta}\right|\right)^2} \tag{3}$$

Where $\hat{\Theta}$ is the prediction value, Θ the observed value and $\overline{\Theta}$ the mean of observed values.

2.3. Theoretical framework

In the same perspective as the work of Dealbera et al. (2024), we consider unidirectional wave propagation along a reference cross-shore x-axis, addressed in a frequency-integrated approach over the short-wave (SW) band. When averaged over many wave cycles, the wave energy flux balance in the absence of mean current can be written as:

$$\frac{\partial E C_g}{\partial x} = \overline{\varepsilon_t} \tag{4}$$

where E is the wave energy, C_g the wave group velocity and $\overline{\varepsilon_t}$ is the total wave-averaged dissipation. E and C_g are estimated by the linear theory formulations for irregular waves:

$$E = \frac{\rho g}{8} H_{rms}^2 \tag{5}$$

with ρ is the density of the water and g the acceleration of gravity and

$$C_g = \frac{1}{2}\left(1 + \frac{2kD}{\sinh(kD)}\right)\frac{\omega}{k} \tag{6}$$

where k and ω are the wave number and the angular frequency associated with the peak period and D the water depth.

$\overline{\varepsilon_t}$ combines the effect of breaking dissipation $\overline{\varepsilon_b}$ and frictional dissipation $\overline{\varepsilon_f}$:

$$\overline{\varepsilon_t} = \overline{\varepsilon_b} + \overline{\varepsilon_f} \tag{7}$$

Following previous experiments in the same flume (Sous et al., 2021), frictional dissipation is expected to be negligible in the smooth RF reference case. For rough seabed cases, the frictional dissipation is overwhelmed by bottom friction and no sidewall dissipation is considered.

The study of non-linear energy transfers made by Dealbera et al. (2024) showed that, for the worst case scenario of the smooth layout, the contribution of non-linear transfers can be considered negligible compared to the effect of breaking and friction dissipation (typically around 1% of global energy dissipation) and will therefore be neglected for the present analysis.

The Thornton and Guza (1983) breaking model is used to represent breaking wave dissipation for all layouts, with adaptation for the specific wave height distribution $p(H)$ observed in our flume (Dealbera et al., 2024) given by the following formula:

$$p(H) = \frac{2H}{H_{rms}^2} \exp\left[-\left(\frac{H - H_0/4}{H_{rms}}\right)^2\right] \tag{8}$$

Where H is the crest-to-trough wave height and H_0 is the spectral root mean square of incident waves measured at the offshore wave gauge.

The rough seabed topography is described for all layouts by a Digital Elevation Model (DEM) depicting the 2D seabed elevation $\aleph(x, y)$, where y is the coordinate along the longshore direction, with a 0.008m horizontal resolution. The geometric structure of the roughness, hereafter referred as to $\psi_\aleph$, can be characterized by a set of metrics (see reviews of Chung et al. (2021); Sous et al. (2024). In the present study, we focus on the standard deviation of seabed elevation $\sigma_\aleph$ and the bulk porosity $n_\aleph$ given by the following formulas:

$$\sigma_\aleph = \sqrt{\frac{1}{n}\sum_i^n \left(\aleph_i - \overline{\aleph}\right)^2} \tag{9}$$

$$n_\aleph = 1 - \frac{\sum\left(\sum \max\left(\aleph(x,y), 4\sigma_\aleph\right)\Delta y\right)\Delta x}{L_x L_y 4\sigma_\aleph} \tag{10}$$

$$\tag{11}$$

Their values are given in Appendix B.

2.4. Wave energy dissipation models

Two wave dissipation models are assessed and compared: the BS model and the BCD model.

2.4.1. The bottom stress model

The SW-integrated BS model follows the previous analysis of Dealbera et al. (2024) on the same experimental database, based on the seminal work of TG83, followed by Lowe et al. (2005a); Péquignet et al. (2011) and others, which defines the frictional dissipation term as:

$$\overline{\varepsilon_f} = \frac{1}{2}\rho f_w |u_{ref}|^3 \tag{12}$$

where u_{ref} is the reference velocity, taken as the standard near-bed velocity for BS models, i.e. at reference depth $D_{ref} = D$. For irregular waves, u_{ref} is generally inferred from the linear wave theory, leading to:

$$\overline{\varepsilon_f} = \frac{\rho f_w}{4\sqrt{\pi}} \left(\frac{\pi H_{rms}}{T_{m01} \sinh kD_{ref}} \right)^3 \tag{13}$$

where T_{m01} is the average wave period and k the wave number associated with T_{m01}.

Following Swart (1974); Madsen et al. (1988); Nielsen (1992), the wave friction factor f_w is related to the ratio of the wave orbital excursion at the bottom to a typical vertical roughness scale, the so-called hydraulic roughness k_r (or equivalent Nikuradse roughness height), through the following expression:

$$f_w = \exp\left(a_1 \left(\frac{A_{ref}}{k_r} \right)^{a_2} + a_3 \right) \tag{14}$$

where a_1, a_2 and a_3 are dimensionless empirical constants taken as 5.0, -0.15 and -5.9 (Sous et al., 2023; Dealbera et al., 2024) and $A_{ref} = u_{o,ref}/\omega$ the bottom orbital excursion with $u_{o,ref}$ the bottom orbital velocity given by the linear theory:

$$u_{o,ref} = \frac{\pi H_{rms}}{T_{m01} \sinh kD_{ref}} \tag{15}$$

2.4.2. The bulk canopy drag model

The base model

The SW-integrated BCD model is based on the work of Mendez and Losada (2004) (ML04), which follows Dalrymple et al. (1984) on an array of immersed cylinders. Energy

loss is estimated using the drag forces induced by the cylinders on the fluid in Morison's equation, neglecting skin friction and inertia:

$$\overline{\varepsilon_f} = \frac{2}{3\pi}\rho C_d A_v \left(\frac{k_p g}{2\omega}\right)^3 \frac{\sinh(k_p\alpha_v D)^3 + 3\sinh(k_p\alpha_v D)}{3k_p\cosh(k_p D)^3} \int_0^\infty H^3 p(H) dH \tag{16}$$

where k is the wave number associated with the peak period T_p, C_d is the bulk drag coefficient, A_v is the transverse frontal area, i.e. the frontal area exposed to the flow divided by the vegetation mean height, and α_v is the relative height of the vegetation given by $\alpha_v D = \overline{h_v}$, where $\overline{h_v}$ is the mean height of roughness blocks. Here the probability distribution of wave heights $p(H)$ is the modified Rayleigh distribution given by Eq. 8.

C_d dependency to local hydrodynamics and roughness structure

The drag coefficient C_d has been shown to depend both on obstacle structure and on local hydrodynamic conditions (Wang et al., 2021). For the former dependency, in order to overcome the standard case of vertical vegetation-mimicking cylinders and to assess the wider applicability of the BCD model, we will simply state that C_d is affected by the roughness geometrical structure $\psi_{\aleph}$. The hydrodynamics control on C_d is generally predicted using dimensionless parameters characterizing the local flow: the Reynolds number $Re = u_c l_v/\nu$ that compares inertial and viscous forces or the Keulegan-Carpenter number $KC = u_c T_p/l_v$ that indicates the relative importance of drag forces over inertia forces, where ν is the kinematic viscosity, l_v the characteristic length of vegetation and u_c is the characteristic velocity acting on the plant and defined as the maximum horizontal velocity at the reference vegetation depth $D_v = D - \alpha_v D$. The early work of Mendez and Losada (2004) proposed a hydrodynamic exponential formulation of C_d versus KC, considering the α_v ratio. Since then, power-law formulation for C_d have been largely used (Wang et al., 2021):

$$\begin{aligned} C_d = &\quad a_{Re}\,(1 + (b_{Re}/Re)^{c_{Re}}) \\ C_d = &\quad a_{KC}\,(1 + (b_{KC}/KC)^{c_{KC}}) \end{aligned} \tag{17}$$

where a_{Re}, b_{Re}, c_{Re}, respectively a_{KC}, b_{KC}, c_{KC} are empirical parameters for Re-based and KC-based models, respectively. Wide ranges of values have been proposed for these parameters (Wang et al., 2021), with dependency on wave forcing, vegetation characteristics and methodology (in particular the definition of u_c and l_c).

Aiming to provide a more unified view of the canopy drag approach possibly extended to rocky or coral seabeds, we propose to discriminate the contributions of canopy geometry and hydrodynamics in the power-law C_d formulations by introduction f_d, a drag factor solely controlled by roughness structure:

$$\begin{aligned} C_d = &\quad f_{d,Re}(\psi_{\aleph}) a_{Re} \left(1 + (b_{Re}/Re)^{c_{Re}}\right) \\ C_d = &\quad f_{d,KC}(\psi_{\aleph}) a_{KC} \left(1 + (b_{KC}/KC)^{c_{KC}}\right) \end{aligned} \tag{18}$$

Here the a, b and c parameters are been assumed to be universal for a selected dimensionless parameter, i.e., the geometry dependency can be fully represented by f_d while the hydrodynamical control is fully accounted for by the power-law. The coefficient values used hereafter have been retrieved from three selected studies of the standard vegetation approaches Koftis et al. (2013); Anderson and Smith (2014); Chastel et al. (2020), hereinafter named K13, A14 and C20 respectively, that cover a large range of Re and KC values for irregular waves. In addition, representative average values, hereafter named D24, have been extracted by fitting a compiled dataset from published experiments and numerical models (Mendez et al., 1999; Mendez and Losada, 2004; Wu and Shu, 2011; Koftis et al., 2013; Anderson and Smith, 2014; Chastel et al., 2020; van Veelen et al., 2020). The parameter values for K13, A14, C20 and D24 together with their ranges of hydrodynamical regimes are presented in Table 1.

Reference	a_{Re}, b_{Re}, c_{Re}	a_{KC}, b_{KC}, c_{KC}	**Hydrodynamical regimes**
K13	0, 2400, 0.77	-	$1000 < Re < 3500$
A14	0.76, 744.2, 1.27	1.10, 27.4, 3.08	$533 < Re < 2296$ $26 < KC < 112$
C20	1.56, 1644, 1.26	2.23, 30.1, 1.37	$500 < Re < 3500$ $15 < KC < 170$
D24	0.25, 2500, 1	0.7, 192, 0.8	$213 < Re < 1600$ $1 < KC < 166$

Table 1: Summary of empirical formulations proposed for the BCD model coefficients.

Geometric vs topographic approaches

Studies of wave damping by vegetation have mainly based their calculations of characteristic dimensions on idealized geometries, such as cylinder and cube networks. However, in the context of natural topography observed over coral reefs and rocky platforms, geometrical parameters are hardly identified since neither repeated patterns are present (not even a dominant roughness wavelength (Stewart et al., 2019; Duvall et al., 2019; Sous et al., 2020, 2024)) nor identifiable isolated elements of roughness. We develop in this study two approaches based on different conceptions of roughness.

- *the geometric approach* based on the classical strategy developed for vegetation studies

on regular arrays of idealized obstacles. The canopy structure parameters are here directly inferred from the obstacle dimensions.

- *the topographic approach* which aims to be applicable to natural rough sites. The terrain is here described in terms of statistical or bulk properties, without any assumption on the presence of regularly spaced and easily measurable obstacles.

The geometric approach reuses the classical parameters given in the review of Wang et al. (2021): l_c is taken as b_v, the stem diameter of the roughness blocks, which gives an estimation of $A_v = b_v N_v$, where N_v is the density of the blocks. The $\overline{h_v}$ height is calculated as the mean of all roughness block heights.

For the topographic approach, the difficulty is to establish an equivalent for A_v in equation 16 usable in natural terrain. The method used here is based on the solid volume calculation. For idealized geometries, the solid volume is expressed as follows:

$$V_{solid} = b_v^2 h_v N_v S \tag{19}$$

where h_v is the block height and S is the plane reference surface. For a natural topography, the solid volume can be expressed as follows:

$$V_{solid} = \int_x \int_y \max\left(4\sigma_{\aleph}, \aleph(x,y)\right) dxdy \tag{20}$$

Considering the equivalence between both expressions of solid volume given by Eq. 19 and 20, a proxy for $b_v N_v$ can be estimated for natural terrain:

$$b_v N_v = \frac{\int_x \int_y \max\left(4\sigma_{\aleph}, \aleph(x,y)\right) dxdy}{b_v h_v S} = \frac{1 - n_{\aleph}}{b_v} \tag{21}$$

We then assume that a natural terrain (i) has a characteristic maximum height equal to 4 times the standard deviation of the bottom elevation $\sigma_{\aleph}$ and (ii) has a horizontal roughness scale equivalent to its vertical scale (isotropy), i.e. $4\sigma_{\aleph}$. Note that the latter hypothesis is rather weak, considering the absence of a dominant horizontal length scale in most natural rough seabeds (Sous et al., 2024). However, the necessary introduction of roughness isotropy at this stage should be, at least partly, compensated by the later inclusion of bottom elevation statistics in C_d and f_d parameters, allowing the introduction of distortion between horizontal and vertical scaling of the roughness. The calculation of A_v is therefore simplified as follows:

$$A_v = \frac{1 - n_{\aleph}}{4\sigma_{\aleph}} \tag{22}$$

Table 2 summarizes the definitions of the different calculated parameters for both BCD approaches.

Approach	A_v	l_c	h_v
Geometric	$b_v N_v$	b_v	$\overline{h_v}$
Topographic	$(1-n_\aleph)/4\sigma_\aleph$	$4\sigma_\aleph$	$4\sigma_\aleph$

Table 2: BCD approach parameters.

2.5. Procedure summary

For each wave run and rough seabed layout, after estimating total incident dissipation from Eq. 4 and subtracting breaking dissipation modeled by the TG83 model, both dissipation models, i.e. the BS model and the BCD model, are optimized. Performances of each model are calculated by comparing the profiles of reconstructed H_{rms} from Eq. 7 to the measured H_{rms} profiles, aiming to maximize WI and to minimize NRMSE. The optimization uses the frictional parameters as free parameters. For the BS model, the wave friction f_w is the free parameter. For the BCD model, three optimizations are performed:

- an optimization directly on C_d, assuming C_d to be spatially uniform for a given wave/seabed case, i.e. without any dependency on hydrodynamics;
- an optimization on $f_{d,Re}$, assuming that C_d varies along the beach profile due to the evolution of local hydrodynamics and that the dependency to hydrodynamics can be represented by Re-based power-law formulation (Eq. 18);
- similarly, an optimization on $f_{d,KC}$, assuming that C_d varies along the beach profile due to the evolution of local hydrodynamics and that the dependency to hydrodynamics can be represented by KC-based power-law formulation (Eq. 18).

The three optimizations are performed for both geometric and topographic approaches. Optimizations of Re- and KC-dependent models are performed using K13, A14, C20 and D24A and A14, C20 and D24 parameterizations, respectively. A summary of the optimization strategy for the BCD model is depicted in Figure 2.

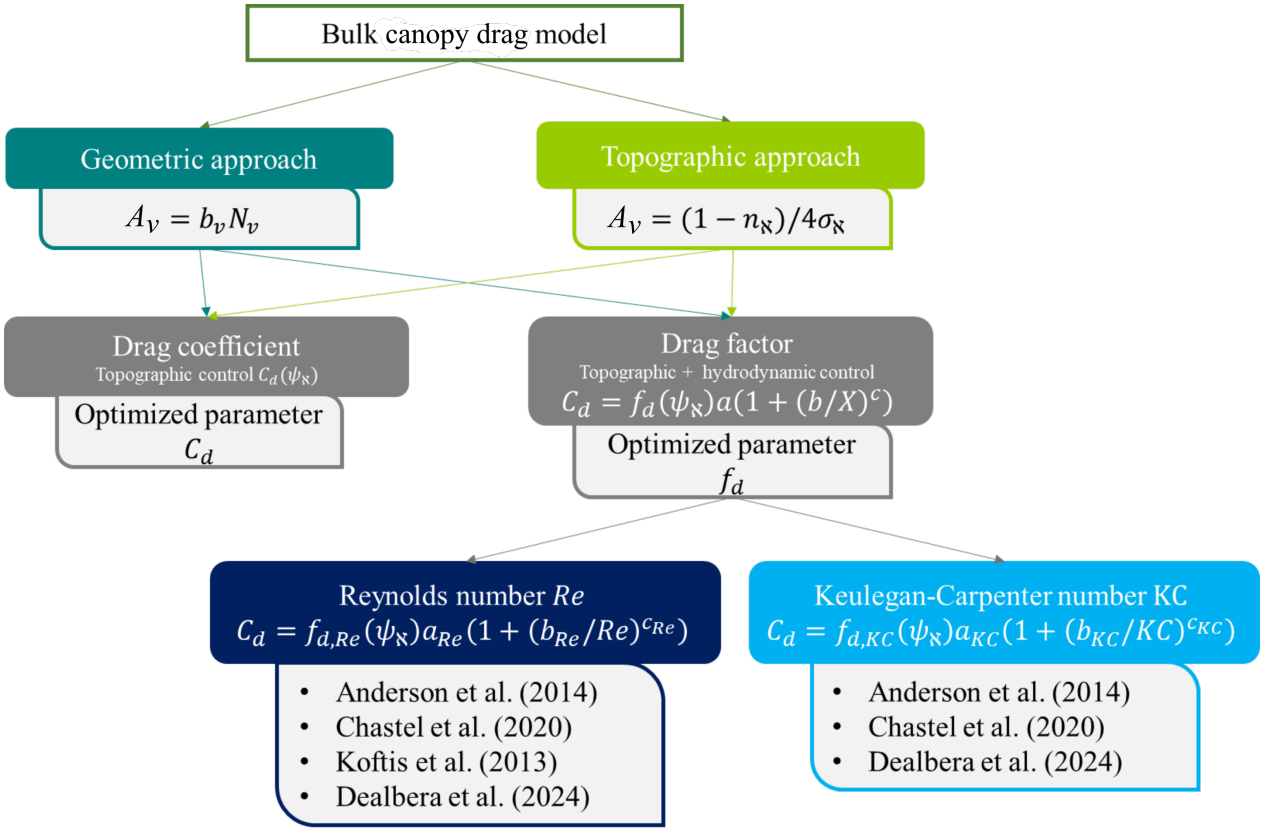

Figure 2: Summary of BCD tests: transverse frontal area A_v approaches in green, optimized parameters in grey and hydrodynamics parameterizations in blue.

3. Results

In this section, we compare the performances of optimizations in order to establish relevant valid parameterizations for the comparison between the two models. We focus first on the BCD model, comparing geometric and topographic approaches, and then assessing Re and KC-based parameterizations for the BCD topographic model. Then, the BS and BCD model performances are compared w.r.t. the hydrodynamical context. Lastly, a comparison between different parameterizations is performed to identify which coefficients fit our data the best.

3.1. BCD model: geometric vs topographic approaches

The first step of the analysis is to assess the robustness of our topographic approach vs the standard geometric approach. The assessment is carried out on three models: uniform C_d, $f_{d,Re}$ and $f_{d,KC}$ with D24 parameterization. Figure 3 displays compared boxplots for NMRSE (left) and WI (right).

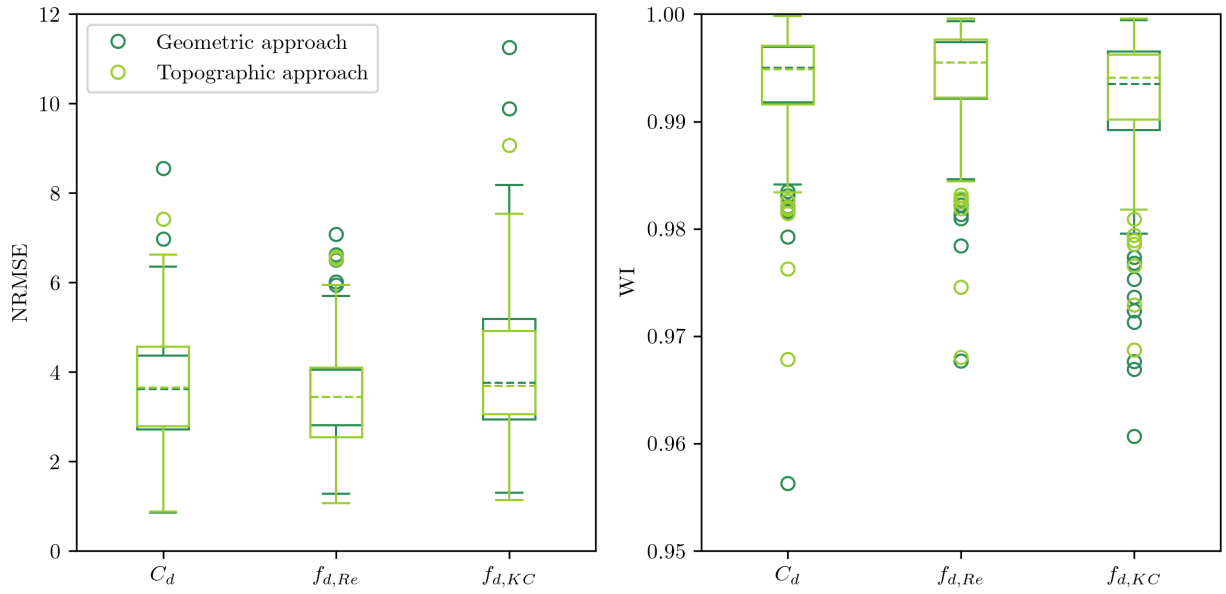

Figure 3: Boxplots of NRMSE (left side) and WI (right side) for the BCD geometric (dark green) and topographic (light green) approaches versus the C_d, $f_{d,Re}$ and $f_{d,KC}$ optimizations. The central dotted line is the median, the edges of the box are the 25 and 75-th percentiles, the whiskers extend to 1.5 of the interquartile range while the outliers are plotted individually as circles.

A first overview shows that the best results (low NRMSE, high WI) for both approaches are obtained for the $f_{d,Re}$ optimization, with median NRMSE and WI of about 3.5% and 0.996. A slight degradation of performances is observed for the C_d and $F_{d,KC}$ respective optimizations but the accuracy remains correct with median NRMSE and WI of about 3.7% and 0.995, 3.8% and 0.994 respectively. The comparison between the geometric (dark green) and topographic (light green) approaches does not outline straightforward differences for each optimization strategy. The performances are slightly enhanced for the geometric approach in C_d optimization, while the topographic approach gives better adjustment for the $f_{d,Re}$ optimization and reduced spread for the $f_{d,KC}$ optimization. Overall, the performance being very similar between topographic and geometric approaches, we will focus on the former one owing to its potential to apply on real terrain.

3.2. BCD model: sensitivity to parameterization

A second series of tests is performed on the topographic approach by comparing performance estimators for different parameterizations. The analysis depicted in Figure 4 focuses on $f_{d,Re}$ and $f_{d,KC}$ optimizations using D24, A14 and C20 parameterizations.

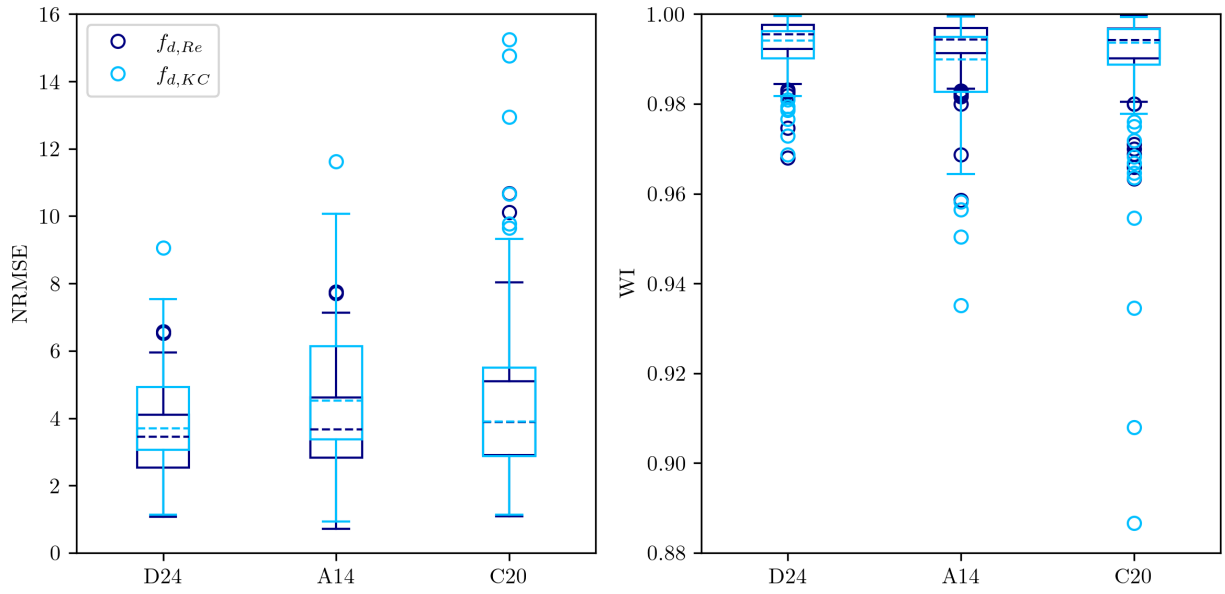

Figure 4: Boxplots of NRMSE (left side) and WI (right side) for the BCD $f_{d,Re}$ (dark blue) and the BCD $f_{d,KC}$ (light blue) versus the D24, A14 and C20 parameterizations. The central dotted line is the median, the edges of the box are the 25 and 75-th percentiles, the whiskers extend to 1.5 of the interquartile range while the outliers are plotted individually as circles. Note the changes in the y-axis.

At first glance, we note better performances for $f_{d,Re}$ parameterizations (dark blue) than for $f_{d,KC}$ ones (light blue). While medians of NRMSE and WI for the D24 and A14 are better for the $f_{d,Re}$ parameterizations, the C20 parameterization displays the same median (3.9% for NRMSE and 0.994 for WI) but a greater spread for the outliers. NRMSE and WI respectively stay below 8% and over 0.98 respectively for the $f_{d,Re}$ parameterizations, but reach over 10% and below 0.98 for the $f_{d,KC}$ ones. Considering that the $f_{d,KC}$ formula gives poorer performance for each selected parameterization, the following analysis will be focused on the $f_{d,Re}$ approach.

3.3. Friction dissipation model comparison

The previous analysis demonstrated (i) the relevancy of the topographic approach for the BCD model and (ii) the prevailing performance of *Re*-based parameterization. The next step is to compare performance estimators for the BS, the C_d- and the $f_{d,Re}$-optimized BCD models, depicted in Figure 5 in brown, light green and dark blue, respectively. We first test the agreement between experiments and model against the $A_o/\sigma_{\aleph}$ ratio, in order to explore the potential degradation of the predictive capacities for large relative roughness height. For all models, the best results are obtained for the $A_o/\sigma_{\aleph} > 2.5$, with similar values of the

estimators as the NRMSE remains lower than 3.2 % and WI higher than 0.996. A degradation of the performance is observed as $A_o/\sigma_{\aleph}$ decreases but the accuracy remains correct, with NRMSE and WI below 10% and over 0.96, respectively, in the 0.0-1.0 interval. For each $A_o/\sigma_{\aleph}$ interval, the BS model displays the lower performance as the medians in NRMSE and WI are around 4.4% and 0.996 for the 1.2-2.5 interval and around 5.4% and 0.990 for the 0.0-1.0 interval. The C_d-optimized BCD model shows better performance for small values of $A_o/\sigma_{\aleph}$ and yet taking into account local hydrodynamics with the $f_{d,Re}$-optimized BCD model improves performances as the medians in NRMSE and WI are around 3.4% and 0.996 for the 1.2-2.5 interval and around 3.9% and 0.995 for the 0.0-1.0 interval.

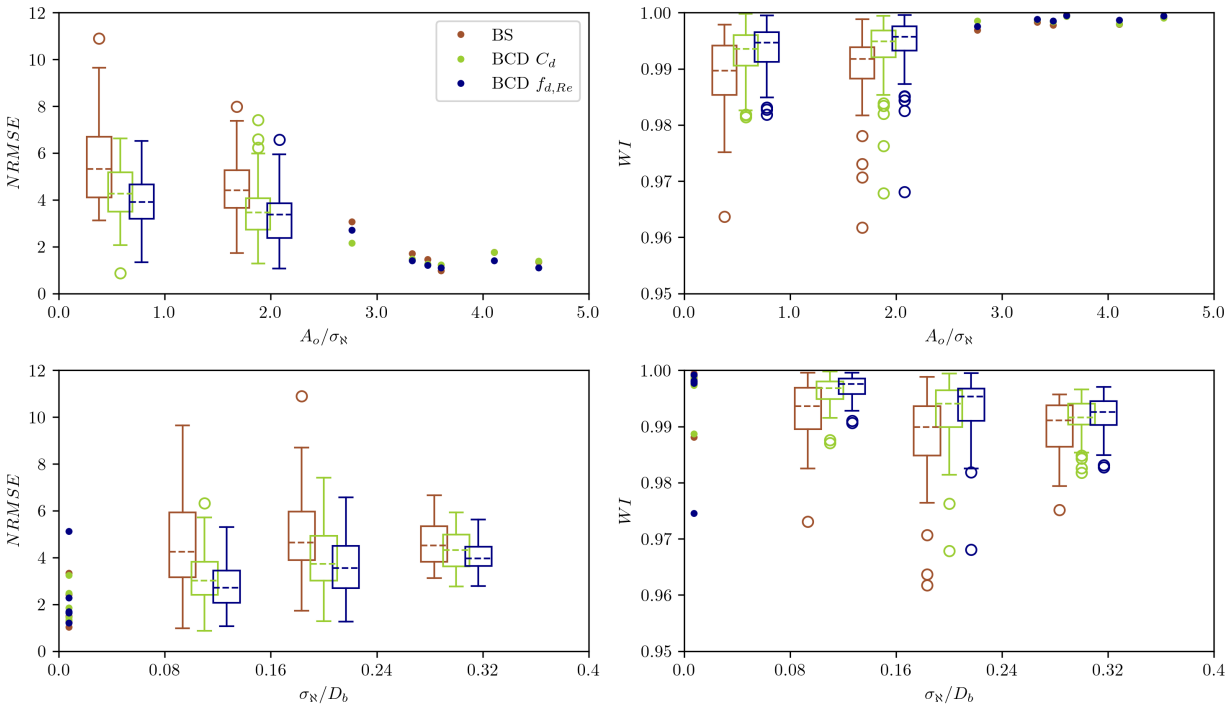

Figure 5: Plot and binned boxplots of NRMSE and WI versus $A_o/\sigma_{\aleph}$ for the following intervals : [0,1.16,2.6] and $\sigma_{\aleph}/D_b$ for the following intervals : [0.07,0.15,0.25,0.35]. The central dotted line is the median, the edges of the box are the 25 and 75-th percentiles, the whiskers extend to 1.5 of the interquartile range while the outliers are plotted individually as circles. Single points are individual datapoints. The BS model is represented in brown, the BCD topographic C_d model in light green and the BCD topographic $f_d(Re)$ model in dark blue. Note that the abscissa values for boxplots have been slightly shifted to improve visibility but presented data has been obtained with similar $A_o/\sigma_{\aleph}$ and $\sigma_{\aleph}/D_b$

A second series of tests is performed on the relative roughness submergence ratio, i.e. the ratio between roughness height and local depth, which becomes an important parameter

for frictional dissipation in rough shallow areas (Davis et al., 2021). The submergence ratio being variable across the profile in our sloping beach configuration, the breaking point value $\sigma_{\aleph}/D_b$ is used, where D_b is the breaking depth obtained at $H_{rms}/D_b \approx 0.7$ (Symonds et al., 1995). The best results are obtained for the smallest $\sigma_{\aleph}/D_b$ for each model. The BS model shows degrading performances for higher $\sigma_{\aleph}/D_b$ with NRMSE and WI medians around 4.2% and 0.993 in the 0.08-016 interval. However, the performance remains rather stable and does not strongly drop for high submergence ratios. Overall, the C_d-optimized BCD model gives better results than the BS model, but $f_{d,Re}$-optimized model is once again more efficient. We note a slight degradation of performance with higher $\sigma_{\aleph}/D_b$ as NRMSE and WI median move from 2.8% and 0.998 in the 0.08-0.16 interval to 4.0% and 0.993 in the 0.24-0.40 interval, drawing closer to the BS and C_d-optimized BCD models.

3.4. BCD hydrodynamic parameterization comparison

The previous results demonstrate the overall superiority of $f_{d,Re}$-optimized BCD model over other approaches. The question arises then on the performance of the formulation proposed here from a compilation of published studies (D24 in Table 1) w.r.t selected references (K13, A14 and C20 in Table 1). Compared NRMSE and WI are depicted in Figure 6.

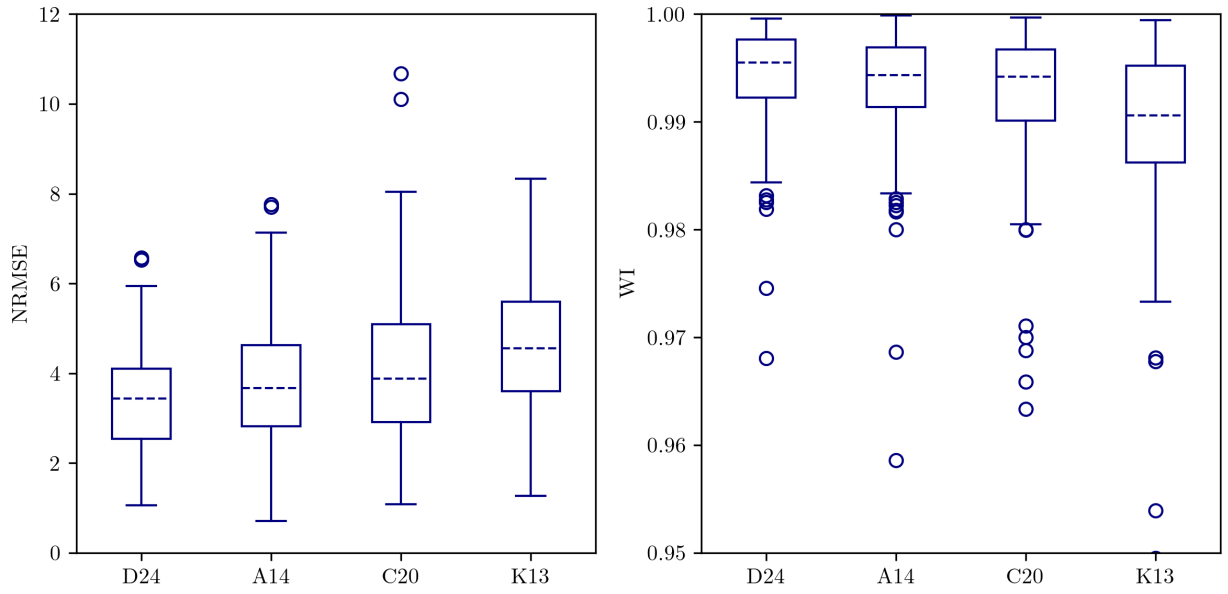

Figure 6: Boxplots of NRMSE (left side) and WI (right side) for the BCD $f_{d,Re}$ (dark blue) versus the D24, A14, C20 and K13 parameterizations. The central dotted line is the median, the edges of the box are the 25 and 75-th percentiles, the whiskers extend to 1.5 of the interquartile range while the outliers are plotted individually as circles.

A clear performance increase is brought by D24 compared to other study-specific parameterizations. A strong improvement is observed when comparing D24 to K13 parameterization, leading to a median NRMSE decrease from 4.60% to 3.43% and a median WI increase from 0.991 to 0.996. Slightly weaker improvements are observed when comparing D24 to A14 and C20, but the overall trend remains satisfactory for D24.

4. Discussion

4.1. Synthesis of the findings

Based on laboratory experiments, the present study aimed to identify the most robust approach to describe wave dissipation over macro- and mega-rough terrain in phase-averaged wave models. The main finding is that, once each model has been carefully optimized, the bulk drag canopy model consistently shows better predicting capacities than the bottom stress model, which is in agreement with their respective theoretical frameworks. The inclusion of local hydrodynamics in the drag coefficient improves the model performance, in particular considering the compiled Re-based formulation proposed here.

4.2. BCD model: the role of roughness architecture

In order to gain further insight into the role played by roughness architecture, a local analysis of the topographic approach has been performed. Local values of C_d are inferred along the beach profile, combining Equations 7 and 16 for each wave run and roughness layout case. The retrieved C_d data has been bin-averaged logarithmically-spaced Re and KC bins depending on the tested formulation. Figure 7 displays the bin-averaged C_d vs Re (left plot) and KC (right plot), while the color/symbol code depicts the different seabed layouts. The experimental bin-averaged drag coefficient ranges from 0.12 to 8.84.

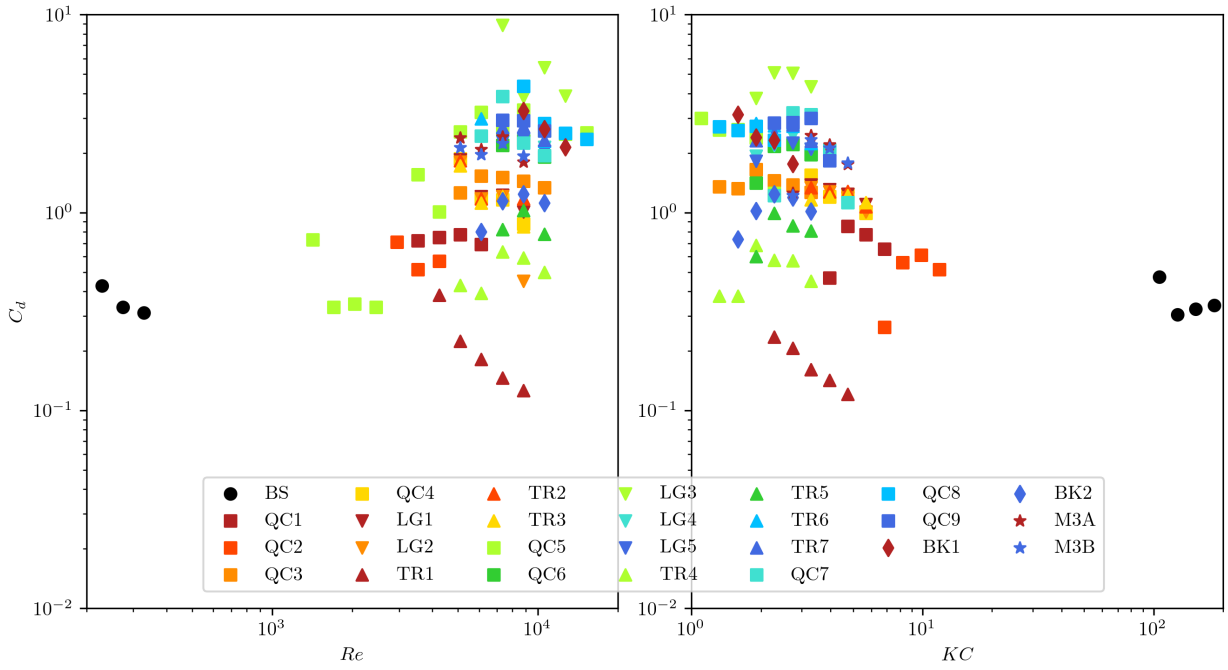

Figure 7: Bin-averaged values of measured C_d plotted as a function of Re (left side) and KC (right side) colored by seabed layouts.

We observe for each layout an overall decrease in C_d in response to an increase in Re or KC which is consistent with the existing power law formulation. However, a striking variability is observed between the different layouts for given Re or KC. This emphasizes the need for establishing a roughness-dependent drag factor f_d. The qualitative analysis from a closer look at Figure 7 underlines the effect of the plane solidity by comparing the BK1, QC6 and BK2 layouts which have decreasing skewness. The smaller the skewness is, the higher the C_d is. The directionality effect is assessed by comparing the LG3, QC6 and TR5, which shows that longitudinal/transverse alignments produce an increase/decrease of drag for the same statistical moments. This observation may appear contradictory with the findings of Dealbera et al. (2024) on the wave friction factor, which demonstrates higher frictional dissipation for transverse anisotropic roughness systems when compared to longitudinally oriented ones. This apparent contradiction must be interpreted keeping in mind that roughness metrics are already involved in the definition of A_v, which indicates that a higher C_d does not systematically indicate a higher drag force. More generally, though the effects of those metrics can be visually identified for contrasted architecture, no simple relationship between f_d and the dimensionless metrics of the roughness $\psi_{\aleph}$ has been identified based on the present BCD dataset. The BCD topographic approach proposed here is based

on a unique length scale, $\sigma_{\aleph}$, implicitly assuming that it encompasses the scaling of vertical, longitudinal and transverse dimensions of the roughness geometry. Such assumption likely does not hold for real rough terrains, which are characterized by a fractal structure, i.e. no dominant horizontal length-scales (Duvall et al., 2019; Sous et al., 2020, 2024). If relevant in the present context, this σ-scaling assumption would allow to define the drag factor f_d as a dimensionless parameter, expected to depend on topographical metrics $\psi_{\aleph}$ only. However, the retrieved f_d remains predominantly explained by σ, with 53 % of f_d variability being explained. This likely indicates a shortcoming in the dimensional scaling, which can not be simply unravelled with the present dataset. The secondary explanatory variable is the Directionality index proposed by Dealbera et al. (2024) (20 % explained variability). For practical application, a simple parametric formulation can be proposed to replace the product $A_v f_d$ for the topographic approach by:

$$K(1 - 0.6\Delta)(1 - n_{\aleph}) \tag{23}$$

with K being an empirical dimensional constant optimized here at $60m^{-1}$ and Δ the Directionality index of Dealbera et al. (2024).

Further observations on more realistic terrains, both in the laboratory and on the field, are required to determine if a robust relationship can be established by f_d and non-idealized roughness architecture metrics (Chung et al., 2021; Sous et al., 2024).

4.3. BS model: introducing the canopy top velocity

The BS model, which remains widely used in nearshore spectral wave modeling, shows lower performance than the BCD model. It is worthwhile to mention that the reduction in predicting accuracy remains moderate, of the order of a few percents even for large roughness conditions, even beyond the base theoretical framework. In particular, the use of a reference near-bed flow velocity can be irrelevant in the macro-roughness case, where we can expect that the orbital motion does not fully penetrate the roughness (Tang et al., 2019). Keeping the simplicity of the standard BS model, an alternative definition of the reference flow velocity is tested here, using the velocity estimated at the top of the roughness blocks, as performed in the BCD ML04 model. Equations 13 and 14 are estimated taking now at the reference depth at the canopy top elevation $D_{ref} = D_v = D - \alpha_v D$. The modified model is referred to as the BS-RT approach. Figure 8 displays the comparison between the standard BS and the BS-RT models, similar to the analysis performed in Figure 5.

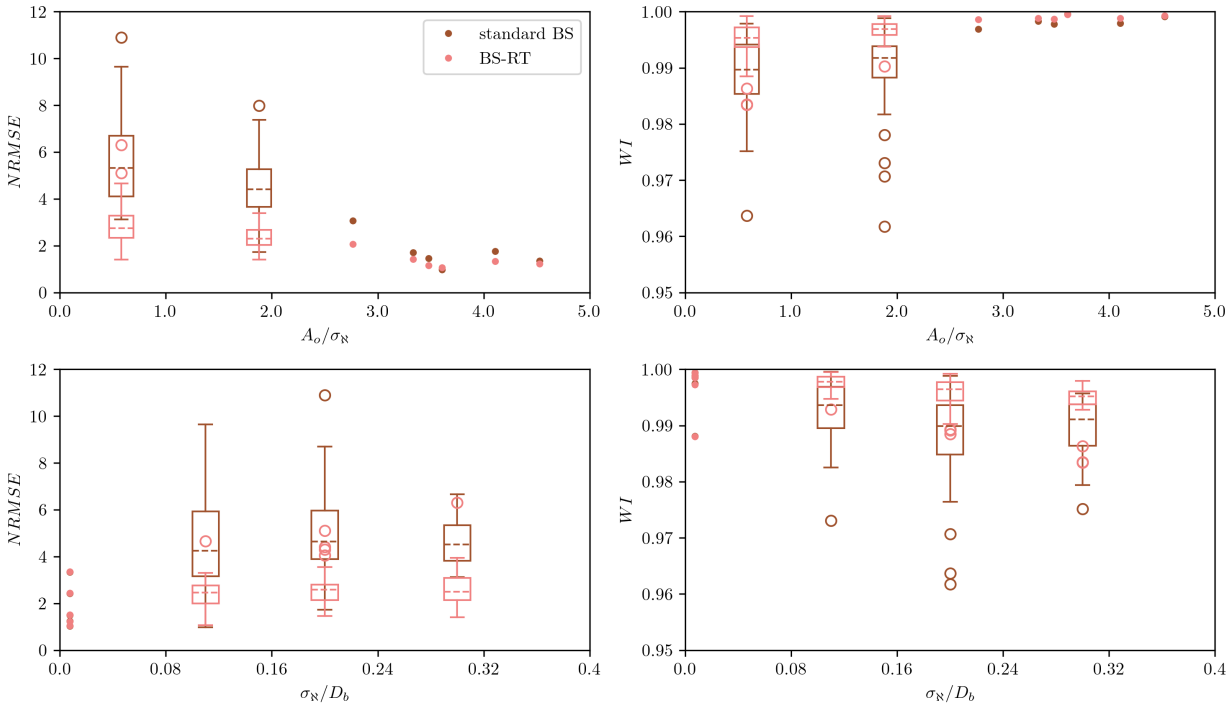

Figure 8: Plot and binned boxplots of NRMSE and WI versus $A_o/\sigma_\aleph$ for the following intervals : [0.30,0.80,1.30,2.00] and $\sigma_\aleph/D_b$ for the following intervals : [0.00,0.30,0.70]. The central dotted line is the median, the edges of the box are the 25 and 75-th percentiles, the whiskers extend to 1.5 of the interquartile range while the outliers are plotted individually as circles. Single points are individual datapoints. The standard BS model is represented in brown and the BS-RT model in red.

A clear improvement is noted for the BS-RT approach against the standard BS approach, with the reduction of the spread of estimators below 6% instead of 10% for the NRMSE and above 0.98 instead of 0.96 for the WI. While already useful for practical applications, further systematic tests on the BS-RT model should be carried out to evaluate the effect of reference depth for the calculation. In particular, the inflexion of the vertical current profile inside and outside the canopy and its dependency on the roughness architecture and/or the local hydrodynamical conditions might affect the parameterization of the reference depth (Lowe et al., 2005b). Note that the BS-RT approach has the potential advantages of being easily tested from simple modified of standard BS formulations, which are already implemented in most spectral models, and being only dependent on external parameters of the system, without requiring knowledge of the internal flow inside and above the canopy Lowe et al. (2007).

4.4. Prospects

The present study is based on a macroscopic description of the roughness canopy, i.e. that the influence of the obstacles on the wave field is spatially integrated. The individual effect of each element is not described by the present modelling approach, which aims to be applicable to typical scales of operational nearshore models. However, the question necessarily arises on the validity of such bulk approaches for large roughness elements scaling as the depth or the wave height, able to induce local reflection and strongly affects the breaking (Sambe et al., 2011). The present results confirm, at the laboratory scale, the robustness of the macroscopic approach throughout the range of tested conditions but the exact limitations remain to be established by high-resolution numerical simulations or experiments.

Following the base works of Dalrymple et al. (1984) and Mendez and Losada (2004), the assumption has been made that the obstacle-induced drag force can be represented by a single quadratic formulation, i.e. implicitly assuming that the turbulent drag largely dominates over laminar and inertial components. Using classical regime diagram (Gu and Wang, 1991; Van Gent, 1993), the turbulence dominance assumption is expected to be validated for most of the tested roughness elements but for the largest ones, a comparable effect of turbulent and inertial drag components is expected, while laminar contribution remains small in each case. The missing inertial drag may likely explain part of the decrease of predictive performance of the BCD model observed for the large roughness cases, corresponding to small $A_o/\sigma_\aleph$ or large $\sigma_\aleph/D_b$ ratios. The implementation of the inertial component of drag is one of the main prospects of the present research works.

5. Conclusion

In very rough environments, bottom-induced wave dissipation is expected to be comparable or even dominant over depth-induced breaking dissipation. The present study aimed to compare several modeling strategies against the laboratory dataset presented by Dealbera et al. (2024). Two standard models, conventionally named here BS (bottom stress model) and BCD (bulk canopy drag model), are traditionally used to predict the energy dissipation generated by the stress exerted on the flow by irregular seabeds. The first model considers the dissipation inside the bottom boundary layer for small roughness while the second one estimates the drag over the water column portion affected by the canopy. As the BCD model has been mainly implemented for idealized geometry, a new approach called the topographic approach has been developed in this study to extend the model application to real rough (rocky or coral reef) terrain. In addition, the BCD model is assessed by testing either a uniform drag coefficient or a variable drag coefficient controlled by local hydrodynamics parameters, Re and KC through a power-law formulation. Several power-law parameterizations have been tested. The comparisons of the performance estimators between the classical

geometric approach and the topographic approach show similar agreements between the observations and the predictions, while the comparison between the Re- and KC-controlled parameterizations shows a lower performance for the KC-controlled parameterizations. The comparison between the BS and the BCD models underlines the better agreement found for the BCD model for all hydrodynamics conditions explored, though the gap between the two tends to narrow for high submergence ratios. The Re-based formulation obtained from a compilation of published datasets provides the best results. An interesting prospect for the BS model relies on the calculation of the reference velocity at the top of the roughness while the BCD model optimizations call for a deepening of the calculation of the transverse area.

Appendix A: Seabed layout matrix

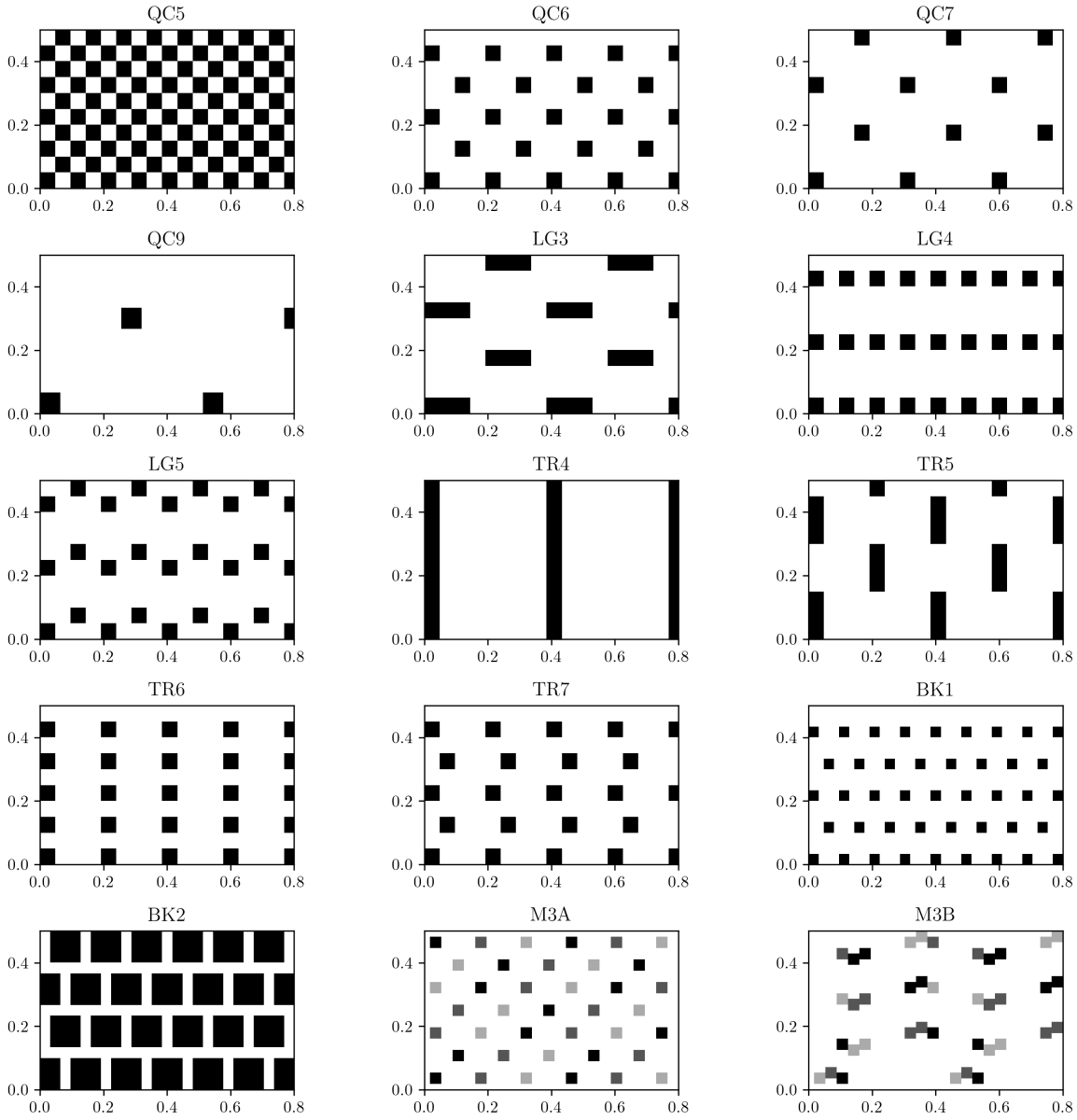

Figure .9: Plane view examples of seabed layouts. x- and y-axes correspond to cross- and along-shore directions. Waves come from the left side. Grey color levels for M3A end M3B indicated the different bloc heights.

Appendix B: Table of seabed layout parameters

Seabed layout name	Block height	$\sigma_א$	$n_א$
RF	0.000	0.000	1.000
BS	0.001	0.000	0.881
QC1	0.016	0.008	0.906
QC2	0.016	0.005	0.750
QC3	0.032	0.016	0.906
QC4	0.032	0.011	0.750
QC5	0.048	0.024	0.906
QC6	0.048	0.016	0.750
QC7	0.048	0.013	0.927
QC8	0.064	0.022	0.900
QC9	0.064	0.015	0.944
LG1	0.032	0.011	0.906
LG2	0.032	0.011	0.906
LG3	0.048	0.017	0.899
LG4	0.048	0.016	0.906
LG5	0.048	0.016	0.906
TR1	0.032	0.012	0.888
TR2	0.032	0.011	0.906
TR3	0.032	0.011	0.906
TR4	0.048	0.016	0.906
TR5	0.048	0.016	0.906
TR6	0.048	0.016	0.906
TR7	0.048	0.016	0.906
BK1	0.064	0.020	0.912
BK2	0.032	0.016	0.728
M3A	0.016 & 0.032 & 0.048	0.012	0.915
M3B	0.016 & 0.032 & 0.048	0.012	0.917

Table .3: Seabed layout metrics.

References

Anderson, M., Smith, J., 2014. Wave attenuation by flexible, idealized salt marsh vegetation. Coastal Engineering 83, 82–92. doi:10.1016/j.coastaleng.2013.10.004.

Chastel, T., Botten, K., Durand, N., Goutal, N., 2020. Bulk drag coefficient of a subaquatic vegetation subjected to irregular waves: Influence of reynolds and keulegan-carpenter numbers. La Houille Blanche 106, 34–42. doi:10.1051/lhb/2020015.

Chung, D., Hutchins, N., Schultz, M.P., Flack, K.A., 2021. Predicting the drag of rough surfaces. Annual Review of Fluid Mechanics 53, 439–471.

Dalrymple, R.A., Kirby, J.T., Hwang, P.A., 1984. Wave diffraction due to areas of energy dissipation. Journal of waterway, port, coastal, and ocean engineering 110, 67–79.

Davis, K.A., Pawlak, G., Monismith, S.G., 2021. Turbulence and coral reefs. Annual review of marine science 13, 343–373.

Dealbera, S., Sous, D., Morichon, D., Michaud, H., 2024. The role of roughness geometry in frictional wave dissipation. Coastal Engineering , 104478doi:10.1016/j.coastaleng.2024.104478.

Dodet, G., Leckler, F., Sous, D., Ardhuin, F., Filipot, J.F., Suanez, S., 2018. Wave runup over steep rocky cliffs. Journal of Geophysical Research: Oceans 123, 7185–7205.

Duvall, M.S., Hench, J.L., Rosman, J.H., 2019. Collapsing Complexity: Quantifying Multiscale Properties of Reef Topography. Journal of Geophysical Research: Oceans 124, 5021–5038. doi:10.1029/2018JC014859.

Farrell, E.J., Granja, H., Cappietti, L., Ellis, J.T., Li, B., Sherman, D.J., 2009. Wave transformation across a rock platform, belinho, portugal. Journal of Coastal Research , 5.

Gon, C.J., MacMahan, J.H., Thornton, E.B., Denny, M., 2020. Wave dissipation by bottom friction on the inner shelf of a rocky shore. Journal of Geophysical Research: Oceans 125. doi:10.1029/2019JC015963.

Gu, Z., Wang, H., 1991. Gravity waves over porous bottoms. Coastal Engineering 15, 497–524. doi:https://doi.org/10.1016/0378-3839(91)90025-C.

Kirezci, E., Young, I.R., Ranasinghe, R., Muis, S., Nicholls, R.J., Lincke, D., Hinkel, J., 2020. Projections of global-scale extreme sea levels and resulting episodic coastal flooding over the 21st century. Scientific reports 10, 1–12.

Kobayashi, N., Raichle, A.W., Asano, T., 1993. Wave attenuation by vegetation. Journal of Waterway, Port, Coastal, and Ocean Engineering 119, 30–48. doi:10.1061/(ASCE)0733-950X(1993)119:1(30).

Koftis, T., Prinos, P., Stratigaki, V., 2013. Wave damping over artificial Posidonia oceanica meadow: A large-scale experimental study. Coastal Engineering 73, 71–83. doi:https://doi.org/10.1016/j.coastaleng.2012.10.007.

Lavaud, L., Pezerat, M., Coulombier, T., Bertin, X., Martins, K., 2020. Hydrodynamics on a rocky shore under moderate-energy wave conditions. Journal of Coastal Research 95, 1473. doi:10.2112/SI95-284.1.

Losada, I., Lara, J., Del Jesus, M., 2016. Modeling the interaction of water waves with porous coastal structures. J. of waterway, port, coastal, and ocean eng., 2016, 142(6): 03116003. doi:10.1061/(ASCE)WW.1943-5460.0000361.

Lowe, R.J., Falter, J.L., Bandet, M.D., Pawlak, G., Atkinson, M.J., Monismith, S.G., Koseff, J.R., 2005a. Spectral wave dissipation over a barrier reef. Journal of Geophysical Research 110, C04001. doi:10.1029/2004JC002711.

Lowe, R.J., Falter, J.L., Koseff, J.R., Monismith, S.G., Atkinson, M.J., 2007. Spectral wave flow attenuation within submerged canopies: Implications for wave energy dissipation. Journal of Geophysical Research 112, C05018. doi:10.1029/2006JC003605.

Lowe, R.J., Koseff, J.R., Monismith, S.G., 2005b. Oscillatory flow through submerged canopies: 1. velocity structure. Journal of Geophysical Research 110, C10016. doi:10.1029/2004JC002788.

Madsen, O.S., 1995. Spectral wave-current bottom boundary layer flows, in: Coastal Engineering 1994, American Society of Civil Engineers. pp. 384–398. doi:10.1061/9780784400890.030.

Madsen, O.S., Poon, Y.K., Graber, H.C., 1988. Spectral wave attenuation by bottom friction: Theory. Coastal Engineering Proceedings 1, 34. doi:10.9753/icce.v21.34.

Marques, O.B., Feddersen, F., MacMahan, J., 2024a. An effective water depth correction for pressure-based wave statistics on rough bathymetry. Journal of Atmospheric and Oceanic Technology .

Marques, O.B., MacMahan, J.H., Feddersen, F., Conlin, M.P., Wilson, G.W., Malila, M., Rosman, J.H., Acevedo-Ramirez, C., Suanda, S.H., 2024b. Observations of wave dissipation by bottom friction on a rough rocky shore., in: 2024 Ocean Sciences Meeting, AGU.

Mendez, F.J., Losada, I.J., 2004. An empirical model to estimate the propagation of random breaking and nonbreaking waves over vegetation fields. Coastal Engineering 51, 103–118. doi:10.1016/j.coastaleng.2003.11.003.

Mendez, F.J., Losada, I.J., Losada, M.A., 1999. Hydrodynamics induced by wind waves in a vegetation field. Journal of Geophysical Research: Oceans 104, 18383–18396. doi:https://doi.org/10.1029/1999JC900119.

Monismith, S.G., Rogers, J.S., Koweek, D., Dunbar, R.B., 2015. Frictional wave dissipation on a remarkably rough reef. Geophysical Research Letters 42, 4063–4071. doi:10.1002/2015GL063804.

Nielsen, P., 1992. Coastal Bottom Boundary Layers and Sediment Transport. volume 4 of *Advanced Series on Ocean Engineering*. WORLD SCIENTIFIC. doi:10.1142/1269.

Ogawa, H., Dickson, M.E., Kench, P.S., 2015. Hydrodynamic constraints and storm wave characteristics on a sub-horizontal shore platform. Earth Surface Processes and Landforms 40, 65–77. doi:10.1002/esp.3619.

Ozeren, Y., Wren, D.G., Wu, W., 2014. Experimental investigation of wave attenuation through model and live vegetation. Journal of Waterway, Port, Coastal, and Ocean Engineering 140, 04014019. doi:10.1061/(ASCE)WW.1943-5460.0000251.

Poate, T., Masselink, G., Austin, M.J., Dickson, M., McCall, R., 2018. The role of bed roughness in wave transformation across sloping rock shore platforms. Journal of Geophysical Research: Earth Surface 123, 97–123. doi:10.1002/2017JF004277.

Péquignet, A.C., Becker, J.M., Merrifield, M.A., Boc, S.J., 2011. The dissipation of wind wave energy across a fringing reef at ipan, guam. Coral Reefs 30, 71–82. doi:10.1007/s00338-011-0719-5.

Quiroga, P.D., Cheung, K.F., 2013. Laboratory study of solitary-wave transformation over bed-form roughness on fringing reefs. Coastal Engineering 80, 35–48. doi:10.1016/j.coastaleng.2013.05.002.

Rogers, J.S., Monismith, S.G., Koweek, D.A., Dunbar, R.B., 2016. Wave dynamics of a pacific atoll with high frictional effects. Journal of Geophysical Research: Oceans 121, 350–367. doi:10.1002/2015JC011170.

Sambe, A.N., Sous, D., Golay, F., Fraunié, P., Marcer, R., 2011. Numerical wave breaking with macro-roughness. European Journal of Mechanics-B/Fluids 30, 577–588.

Soulsby, R., Hamm, L., Klopman, G., Myrhaug, D., Simons, R., Thomas, G., 1993. Wave-current interaction within and outside the bottom boundary layer. Coastal Engineering 21, 41–69. doi:10.1016/0378-3839(93)90045-A.

Sous, D., Bouchette, F., Doerflinger, E., Meulé, S., Certain, R., Toulemonde, G., Dubarbier, B., Salvat, B., 2020. On the small-scale fractal geometrical structure of a living coral reef barrier. Earth Surface Processes and Landforms 45, 3042–3054. doi:10.1002/esp.4950.

Sous, D., Forsberg, P.L., Touboul, J., Nogueira, G.G., 2021. Laboratory experiments of surf zone dynamics under on-and offshore wind conditions. Coastal Engineering 163, 103797.

Sous, D., Martins, K., Tissier, M., Bouchette, F., Meulé, S., 2023. Spectral wave dissipation over a roughness-varying barrier reef. Geophysical Research Letters doi:10.1029/2022GL102104.

Sous, D., Meulé, S., Dealbera, S., Michaud, H., Gassier, G., Pezerat, M., Bouchette, F., 2024. Quantifying the topographical structure of rocky and coral seabeds. Plos One doi:10.1371/journal.pone.0303422.

Stewart, M.T., Cameron, S.M., Nikora, V.I., Zampiron, A., Marusic, I., 2019. Hydraulic resistance in open-channel flows over self-affine rough beds. Journal of Hydraulic Research 57, 183–196. doi:10.1080/00221686.2018.1473296.

Svendsen, I.A., 2005. Introduction to nearshore hydrodynamics. volume 24. World Scientific Publishing Company.

Swart, D.H., 1974. Offshore sediment transport and equilibrium beach profiles .

Symonds, G., Black, K.P., Young, I.R., 1995. Wave-driven flow over shallow reefs. Journal of Geophysical Research 100, 2639. doi:10.1029/94JC02736.

Tang, C., Lei, J., Nepf, H.M., 2019. Impact of vegetation-generated turbulence on the critical, near-bed, wave-velocity for sediment resuspension. Water Resources Research 55, 5904–5917.

Thornton, E.B., Guza, R.T., 1983. Transformation of wave height distribution. Journal of Geophysical Research 88, 5925. doi:10.1029/JC088iC10p05925.

Van Dongeren, A., Lowe, R., Pomeroy, A., Trang, D.M., Roelvink, D., Symonds, G., Ranasinghe, R., 2013. Numerical modeling of low-frequency wave dynamics over a fringing coral reef. Coastal Engineering 73, 178–190. doi:10.1016/j.coastaleng.2012.11.004.

Van Gent, M., 1993. Stationary and oscillatory flow through coarse porous media. Communications on hydraulic and geotechnical engineering, No. 1993-09 doi:urn:NBN:nl:ui:24-uuid:0408e897-5a3d-46a2-ae8c-75b49d990482.

van Veelen, T.J., Fairchild, T.P., Reeve, D.E., Karunarathna, H., 2020. Experimental study on vegetation flexibility as control parameter for wave damping and velocity structure. Coastal Engineering 157, 103648. doi:https://doi.org/10.1016/j.coastaleng.2020.103648.

Vousdoukas, M.I., Ranasinghe, R., Mentaschi, L., Plomaritis, T.A., Athanasiou, P., Luijendijk, A., Feyen, L., 2020. Sandy coastlines under threat of erosion. Nature climate change 10, 260–263.

Wang, Y., Yin, Z., Liu, Y., 2021. Predicting the bulk drag coefficient of flexible vegetation in wave flows based on a genetic programming algorithm. Ocean Engineering 223, 108694. doi:10.1016/j.oceaneng.2021.108694.

Wu, J., Shu, C., 2011. Numerical study of flow characteristics behind a stationary circular cylinder with a flapping plate. Physics of Fluids 23, 073601. doi:10.1063/1.3601484.

Yin, Z., Yang, G., Wang, Y., Qiu, Q., Jiang, X., 2024. Numerical simulations of breaking wave propagation through the vegetation on a slope based on a drag coefficient prediction model. Ocean Engineering 291, 116440. doi:10.1016/j.oceaneng.2023.116440.